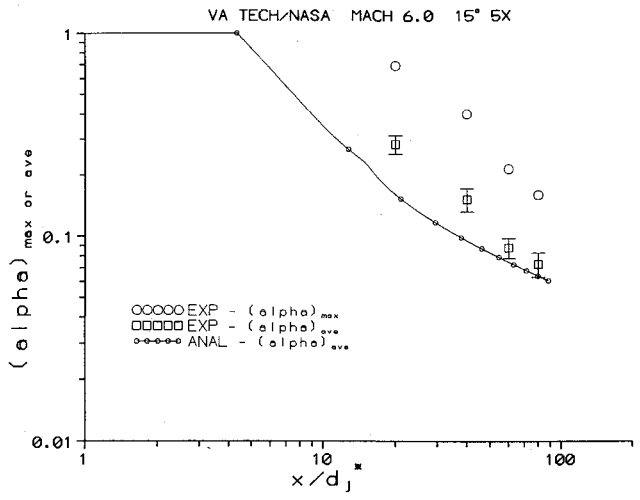

Fig. 4 Comparison of predictions and data for the experiments of Ref. 4 at $M_a = 6.0$ with $\delta_j = 15$ deg.

That is needed to calculate the density and thus the plume cross-sectional area but, most importantly, to calculate the pressure force in the streamwise momentum equation. The model adopted here assumes that Newtonian impact theory can be used to represent the effects of the inclination of the plume to the external flow and to relate the average pressure around the plume to that along the windward stagnation line.

Comparisons with Experiment

The comparisons will be based primarily on the decay of concentration of injectant fluid in the plume. The data is usually reported as the decay of the maximum concentration in the plume at any axial station, and the analysis predicts the one-dimensional average concentration in the plume. Seldom is enough information given to permit relating the maximum to the average concentration. The experiments in Ref. 4 did have enough information, and that implies $\alpha_{ave}/\alpha_{max} \approx 0.4$. Thus, the predictions of α_{ave} should be about 40% of the measured α_{max} at the same station.

We start using the $M_a = 4.0$ experiments reported in Refs. 5 and 6. These tests were all for H_2 injected into air at $M_j = 1.0$ and $\bar{q} = 1.0$. Consider the results shown in Fig. 1 looking first at the predictions and data for the single, isolated jets, i.e., $w/d_j^* = \infty$. As desired, the prediction for α_{ave} is roughly 40% of the measured α_{max}. The predictions also mimic the effects of the spacing w/d_j^* shown in the experiments quite well.

This same group of data can also be used to investigate the effects of injection angle. Predictions and data are given in Fig. 2 for injection angles from 30 to 90 deg, all with $w/d_j^* = 6.25$. The analysis predicts the effects of angle reasonably well.

The effects of a lower external stream Mach number can be probed using the $M_a = 1.4$ data of Ref. 7 which had He injection at $M_j = 1.0$. The results of measurements and the present analysis are plotted in Fig. 3. In this case, the ratio of α_{ave} predicted to α_{max} measured is closer to 60% than the 40% value obtained earlier.

The data of Ref. 4 allows testing the predictions of the analysis for a case with a low injection angle of 15 deg, albeit at a high Mach number of $M_a = 6.0$, with He injection at $M_j = 1.7$ and $w/d_j^* = 9.0$. The results are shown in Fig. 4. Here, the ratio of α_{ave} predicted to α_{max} measured is closer to the 40% value obtained earlier for the $M_a = 4.0$ cases. For this experiment, enough data was available to permit an approximate determination of α_{ave}, and those results are also included in Fig. 4 with 10% error bars. The mass flow of external stream fluid in the plume at three axial stations was measured, and those results can be used to approximately infer an entrainment rate. The experimental entrainment rate can then be compared to the entrainment rate predicted by the entrainment model to try and validate that model. The dimensionless entrainment rate obtained from the experiment in the region $60 \le x/d_j^* \le 80$ is 0.14, and the values from the analysis at $x/d_j^* = 60$ and 80 are 0.13 and 0.11, respectively.

References

[1]Billig, F. S., Orth, R. C., and Lasky, M., "A Unified Analysis of Gaseous Jet Penetration," *AIAA Journal*, Vol. 9, No. 6, 1971, pp. 1048–1058.

[2]Schetz, J. A., Hawkins, P. F., and Lehman, H., "Structure of Highly Underexpanded Transverse Jets in a Supersonic Stream," *AIAA Journal*, Vol. 5, No. 5, 1967, pp. 882–884.

[3]Campbell, J., and Schetz, J. A., "Analysis of Injection of a Heated Turbulent Jet into a Cross Flow," NASA TR R-413, 1973.

[4]Fuller, E. J., Mays, R. B., Thomas, R. H., and Schetz, J. A., "Mixing Studies of Helium in Air at High Supersonic Speeds," *AIAA Journal*, Vol. 30, No. 9, 1992, pp. 2234–2243.

[5]Rogers, R. C., "Mixing of Hydrogen Injected from Multiple Injectors Normal to a Supersonic Stream," NASA TN D-6476, 1971.

[6]McClinton, C. R., "The Effect of Injection Angle on the Interaction between Sonic Secondary Jets and a Supersonic Stream," NASA TN D-6659, 1972.

[7] Lee, R. E., private communication, Applied Physics Lab., Laurel, MD, Oct. 1992.

Impingement of Supersonic Jets on an Axisymmetric Deflector

J. K. Prasad‡ and R. C. Mehta§
Vikram Sarabhai Space Centre, Trivandrum 695022, India
and
A. K. Sreekanth¶
Indian Institute of Technology, Madras 600036, India

Nomenclature

De	= nozzle exit diameter
$\boldsymbol{F}, \boldsymbol{G}, \boldsymbol{H}$	= flux vector
M	= Mach number
M_e	= exit Mach number
P	= pressure
P_0	= total pressure
p_a	= ambient pressure
p_e	= exit pressure
p_s	= static pressure
r	= radial coordinate
T	= temperature
t	= time
$\boldsymbol{U}$	= vector of conserved variables
u, v	= axial and radial velocity, respectively
X_c	= distance measured from nozzle exit plane
x	= axial coordinate
ρ	= density

Introduction

THE phenomenon of supersonic jets and their interaction with solid surfaces is found in many engineering applications such as impingement of exhaust from launch vehicles during the liftoff phase, during stage separation of multistage rockets, and VTOL/STOL operation of aircraft, etc.

Many experiments have been carried out to study free jets.[1–4] A comprehensive experimental investigation of supersonic free jets was reported by Love et al.[5] Abdel-Fattah[6] has measured shock cell lengths for supersonic jets coming out of convergent-divergent nozzles in conjunction with schlieren pictures. Solution of parabolized Navier-Stokes equations using the shock capturing method

Received March 13, 1993; revision received Nov. 18, 1993; accepted for publication Dec. 30, 1993.

*Engineer, Aerothermal Test Facilities.
†Engineer, Aerodynamics Division. Senior Member AIAA.
‡Professor, Department of Aerospace Engineering.

for the single- and two-phase supersonic region was presented by Dash and Wolf.[7] The solution of unsteady Euler equations to obtain the flowfield of underexpanded two-dimensional free jets was carried out by Sinha et al.[8] using the finite difference method. Dash et al.[9] have made extensive numerical studies of underexpanded jets. These numerical studies of free jets reveal that the time-marching method can capture the flowfield features of the free jets.

The impingement flowfield produced due to the impingement of underexpanded supersonic jets on inclined and perpendicular flat plates have been extensively studied by Lamont and Hunt.[10] The shadowgraph and surface pressure distribution on a cone due to impingement of axisymmetric jets were investigated by Jennions and Hunt.[11] Most of these experiments were performed to study free jets or impinging jets on solid obstacles like flat plates, cones, and wedges.

In the present paper, experimental and numerical studies are carried out to investigate impingement flowfield produced on a typical axisymmetric jet deflector. The experiments consisted of schlieren flow visualization and measurements of pressure. The present study will be useful for the design of a typical axisymmetric jet deflector during the liftoff phase of a rocket.

Experimental Apparatus

All of the tests were carried out in open jet facility. High-pressure dry air at 4.3 MPa and ambient temperature was supplied through a 150-mm pipe line to the settling chamber and nozzle assembly. A pressure regulating valve was used to control the nozzle operating pressure. The pressure in the settling chamber was continuously monitored using a Bourden pressure gauge and pressure transducer.

The convergent-divergent nozzles were designed for producing jet exit Mach number, M_e of 2.2. The exit diameter De of the nozzle is 23 mm and has a semidivergent angle of 15 deg. The nozzles were made of stainless steel with 20-μ internal surface finish. The facility can be operated continuously at the maximum pressure for about 80 s which is adequate for data acquisition.

The geometrical detail of the axisymmetric model is shown in Fig. 1. The model consists of a cone-apex angle θ_w of 70 deg and a tip bluntness radius R_1 of $0.13De$. Farther downstream a curvature of radius R_2 of $1.2De$ is provided at a location of $r = 0.7De$, where r is the distance measured from the model axis. The deflector has a base diameter of $8De$. The deflector was mounted on a workshop machine table. The deflector was carefully aligned with its base

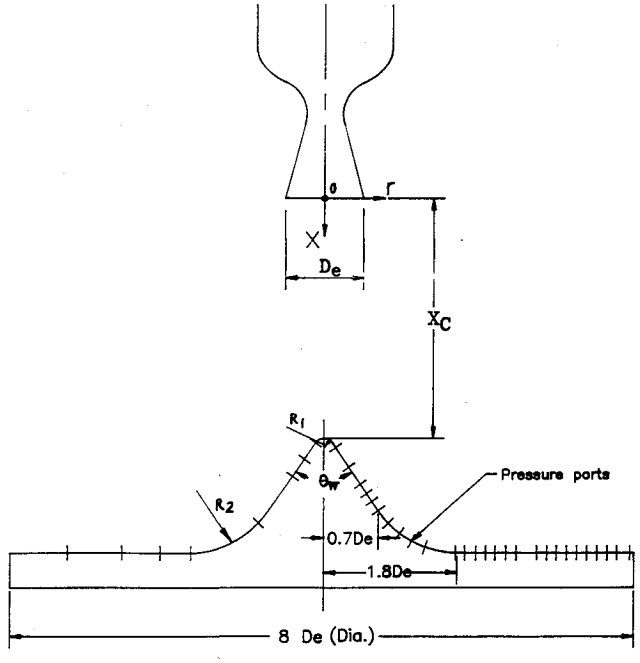

Fig. 1 Details of the axisymmetric deflector model and location of pressure ports.

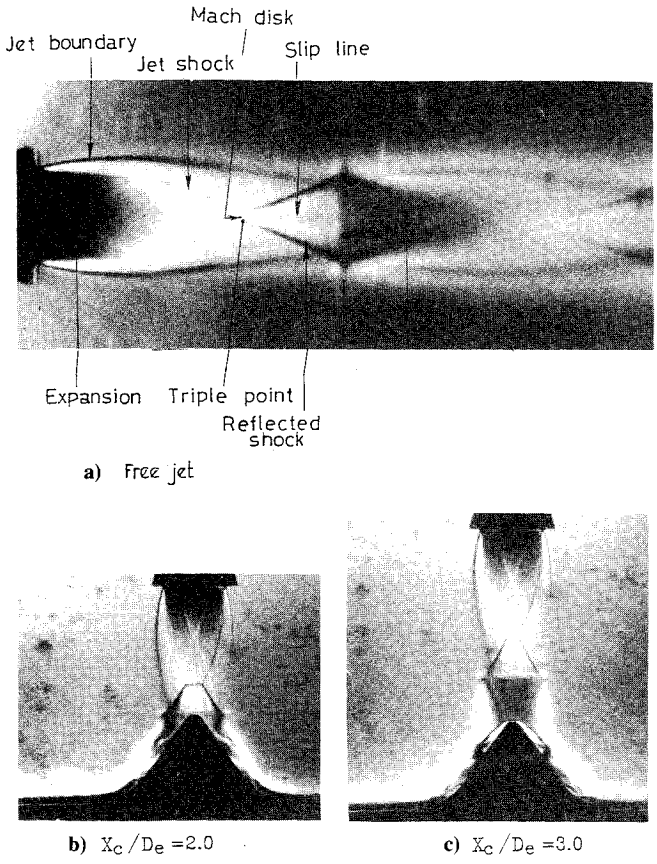

Fig. 2 Schlieren pictures of free jets and impinging jets.

perpendicular to the jet axis, and the apex was centrally located. The process of centralizing the model was accomplished by equalizing the reading from pressure holes at corresponding positions on opposite faces of the deflector.

The maximum diameter of the static pressure probe was 1.52 mm at the aft portion. The probe consists of 40-deg sharp cone at the front end followed by a small taper of 2 deg. Four holes of 0.3 mm diameter are drilled at a distance of 4.89 mm from nose tip for sensing pressure within ± 1% of the nominal value.

The location of pressure orifices is shown in Fig. 1. The measurement of surface pressures were made by making use of a 48-port scanivalve system which houses a pressure tranducer having the range of 0–2 MPa. The pressure tranducer has accuracies better than ±0.1% of the full scale output. All of the data were acquired and processed using a data acquisition system made of analog devices. A single pass, black and white schlieren system was employed for flow visualization photography.

Solution Algorithm

The equations solved are the Euler equations describing the flow of an inviscid, compressible fluid. To allow the capture of shocks and the discontinuous phenomena, the axisymmetric Euler equations are written in conservation vector form as

$$\frac{\partial \boldsymbol{U}}{\partial t} + \frac{\partial \boldsymbol{F}}{\partial x} + \frac{1}{r}\frac{\partial (r\boldsymbol{G})}{\partial r} - \frac{\boldsymbol{H}}{r} = 0 \tag{1}$$

where

$$\boldsymbol{U} = \begin{bmatrix} \rho \\ \rho u \\ \rho v \\ \rho e \end{bmatrix}, \quad \boldsymbol{F} = \begin{bmatrix} \rho u \\ \rho u^2 + p \\ \rho uv \\ (\rho e + p)\, u \end{bmatrix}, \quad \boldsymbol{G} = \begin{bmatrix} \rho v \\ \rho uv \\ \rho v^2 + p \\ (\rho e + p)\, v \end{bmatrix}, \quad \boldsymbol{H} = \begin{bmatrix} 0 \\ 0 \\ -p \\ 0 \end{bmatrix}$$

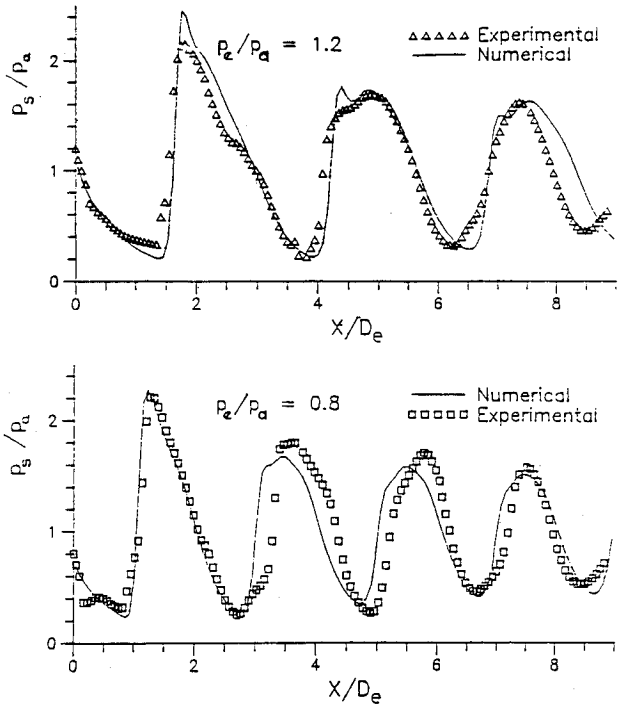

Fig. 3 Comparison of computed and measured free jets static pressure distribution along the jet axis for $M_e = 2.2$.

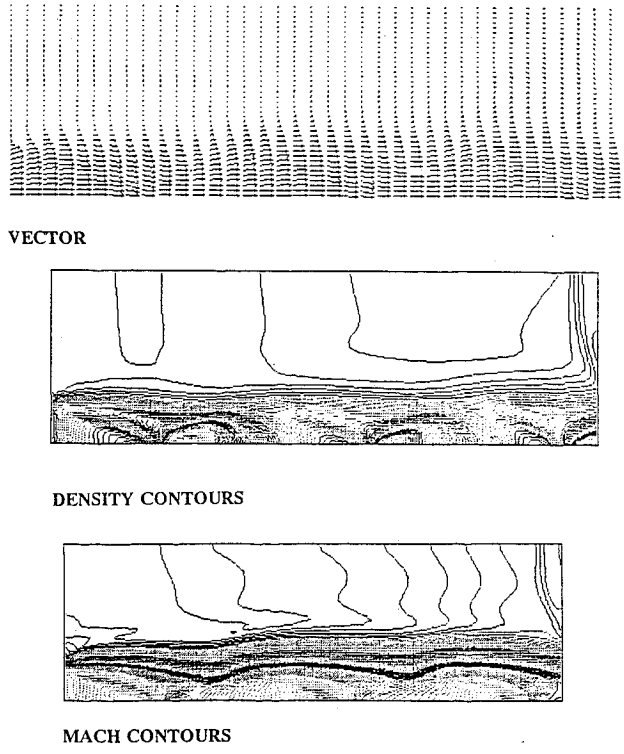

Fig. 4 Vector, density and Mach contours for free jets: $M_e = 2.2$ and $p_e/p_a = 1.2$.

An integral form of Eq. (1) over a finite volume fixed with time is

$$r\frac{\partial}{\partial t}\int \boldsymbol{U}\,\mathrm{d}\Omega + \int_\Gamma (\boldsymbol{F}\,\mathrm{d}r - \boldsymbol{G}\,\mathrm{d}x)\,r - \int_\Omega \boldsymbol{H}\,\mathrm{d}\Omega = 0 \qquad (2)$$

where Ω refers to the axisymmetric domain of volume with boundary Γ. The computational domain is divided into a finite number of quadrilateral cells. The conservative variables within the cells are calculated by their average value at the cell center, and such quantities are denoted by suffixes (i, j). The time marching is performed by using multistage Runge-Kutta integration.[12] Here only two stages are used, giving a second-order accuracy in time

$$\boldsymbol{U}^{n+1/2} = \boldsymbol{U}^n - 0.5\frac{\Delta t}{\Delta A r_c}\sum_{ij}[(\boldsymbol{F}_i\Delta r_i - \boldsymbol{G}_j\Delta x_j)\bar{r} - \boldsymbol{H}_{ij}A_{ij} - D_{ij}] \quad (3a)$$

$$\boldsymbol{U}^{n+1} = \boldsymbol{U}^n - \frac{\Delta t}{\Delta A r_c}\sum_{ij}[(\boldsymbol{F}_i\Delta r_i - \boldsymbol{G}_j\Delta x_j)\bar{r} - \boldsymbol{H}_{ij}A_{ij} - D_{ij}] \quad (3b)$$

where superscript n is the current time level and $n + 1$ is the new time level. Δt is the local time step, r_c the centroid of the cell, $\bar{r}$ the average radial distance of the cell, and A the area of the cell.

In Eqs. (3), D_{ij} are dissipation terms, which are required for suppressing numerical oscillations. The dissipation function[12] consists of a blend of second- and fourth-order difference of the conserved variables U_{ij}. Fourth-order differences are added everywhere in the

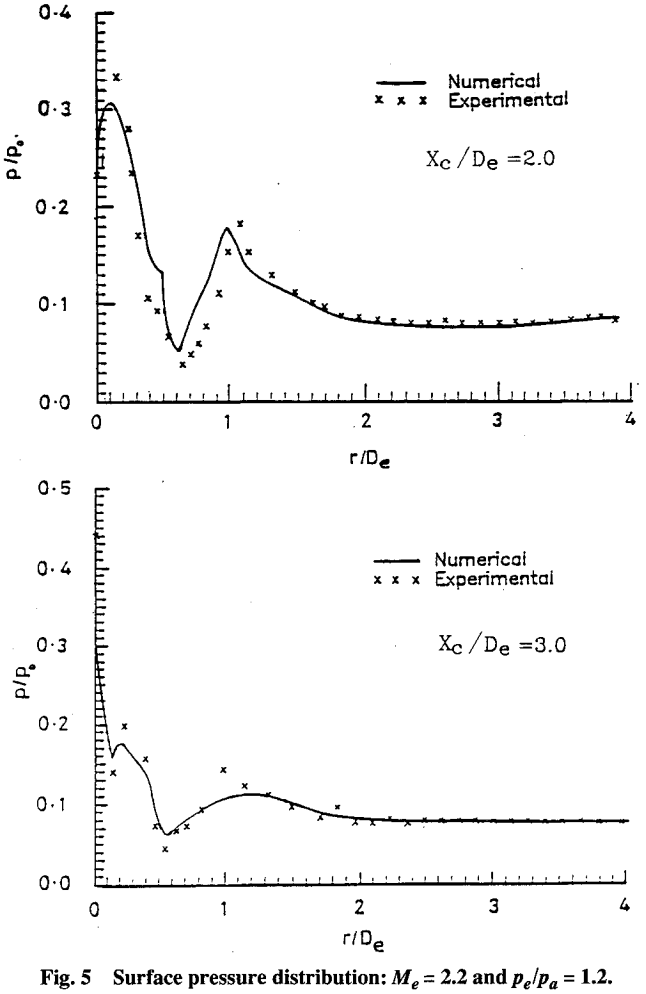

Fig. 5 Surface pressure distribution: $M_e = 2.2$ and $p_e/p_a = 1.2$.

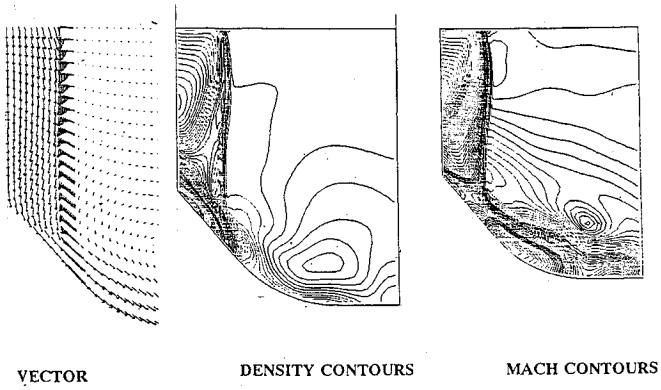

Fig. 6 Vector, density and Mach contours for jet deflector: $M_e = 2.2$ and $p_e/p_a = 1.2$, $X_c/De = 2$.

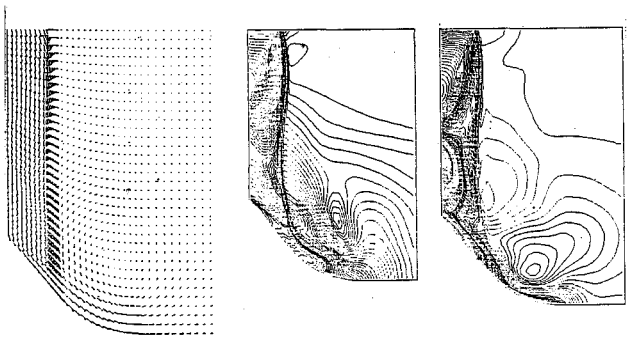

Fig. 7 Vector, density and Mach contours for jet deflector: $M_e = 2.2$ and $p_e/p_a = 1.2$, $X_c/De = 3$.

flow domain where the solution is smooth, but are "switch-off" in the region of shock waves. A term involving second differences is then "switch-on" to damp oscillations near the shock waves. This switching is achieved by means of shock wave sensor, based on the local second differences of pressure.

The numerical computations were done on Landmark i860 base work station with different grid sizes such as 150×40, 200×40 and 150×50.

Results and Discussion

The schlieren picture of the free jets at $M_e = 2.2$ and $p_e/p_a = 1.2$ is depicted in Fig. 2a. The schlieren picture shows most of the flowfield features of the free jets, such as jet boundaries, expansion waves, jet shock, Mach disk, reflected shocks, etc. The impingement flowfield observed through the schlieren system is shown in Figs. 2b and 2c. The flowfield upstream of the cone shock is somewhat similar to that of the free jets as can be seen from the schlieren pictures. It can be seen from the schlieren photograph that the free jets Mach disk has been displaced upstream by about $0.13De$ due to presence of the deflector at $X_c/De = 2$. A weak compression region is observed close to deflector apex. Several compression and expansion zones are observed downstream of the deflector apex. The compression takes place due to the deflector curvature R_2 with an increase in distance, i.e., at $X_c/De = 3$, the jet deflector is now placed in the second shock cell of the free jets. The flowfield has changed appreciably as compared to the flowfield at $X_c/De = 2$. A stronger conical shock has appeared because the incoming jet flow has become supersonic before impinging on the deflector wall.

Figure 3 shows the pressure variation along the jet axis for free jets at $M_e = 2.2$ and $p_e/p_a = 1.2$ and 0.8. The comparison between the experimental and numerical results shows good agreement in pressure distributions along the centerline of the free jets. Figure 4 displays the vector, density, and Mach contours plots for the underexpanded free jet. The shock cells are also visible in the contour plots. Thus, the over all flowfield features of the supersonic free jets is very well captured by present numerical computations.

The static pressure distribution on the deflector surface is nondimensionalized by the settling chamber pressure P_0. The location of the static pressure port on the deflector surface is indicated as the distance r measured from the model axis in the direction normal to it; r is nondimensionalized by the nozzle exit diameter De. The measured static pressure distributions over the jet deflector surface are shown in Fig. 5.

The pressure distribution at $X_c/De = 2$ is shown in Fig. 5a. The stagnation point pressure has a value of 0.232. The static pressure p/P_0 increases marginally to a pressure of 0.305 at $r/De = 0.173$. Further, it starts to decrease to a minimum value of $p/P_0 = 0.0308$ at $r/De = 0.681$, which is below ambient pressure. The pressure further increases due to deflector curvature, attains a peak value of $p/P_0 = 0.1888$ at $r/De = 1.15$, and subsequently falls due to mixing with the ambient condition.

At $X_c/De = 3$, the stagnation point pressure has a higher value of $p/P_0 = 0.44$ as compared to $X_c/De = 2$. The pressure falls rapidly to $r/De = 0.14$ when a small pressure jump is observed, as seen in Fig. 5b. Farther downstream the pressure attains a minimum value of $p/P_0 = 0.04$ at $r/De = 0.55$. The pressure distribution beyond this point is similar to the behavior at $X_c/De = 2$. It can be seen from Fig. 5 that a comparison between experimental and numerical results shows good agreement.

Figures 6 and 7 depict vector, density, and Mach contour plots over the jet deflector. The contours plots exhibit all of the essential flowfield features like Mach disk, jet boundary, expansion and compression waves, cone shock, etc. The comparison of the schlieren pictures of the free jets and impinging jets reveals that the impingement flowfield has similar characteristics of the free jets up to the cone shock of the deflector's apex. The density and Mach contours of the free jets have somewhat similar flowfield features as compared with the density and Mach contours of the impinging flowfield. But the vector plots of the impinging free jets differ appreciably from the impinging vector plots. The pressure distributions above the deflector surface are useful for aerodynamic and structural design.

References

[1]Seiner, J. M., and Norum, T. D., "Experiments of Shock Associated Noise on Supersonic Jets," AIAA Paper 79-1326, July 1979.

[2]Reid, J., and Hasting, R. C., "The Effect of a Central Jet on the Base Pressure of a Cylindrical After Body in a Supersonic Stream," Aeronautical Research Council, Report and Memorandum 3224, London, 1961.

[3]Chiang, C.-H., "Axially Symmetric Supersonic Turbulent Jets Discharged from a Nozzle with Underexpansion," *Turbulent Jets of Air, Plasma, and Real Gas*, Constants Bureau, New York, 1969, pp. 111–137.

[4]Chuech, S. G., Lia, M. C., and Faeth, G. M., "Structure of Turbulent Sonic Underexpanded Jets," *AIAA Journal*, Vol. 27, No. 5, 1989, pp. 549–559.

[5]Love, E. S., Grigsby, C. E., Lee, L. P., and Woodling, N. J., "Experimental and Theoretical Studies of Axisymmetric Free Jets," NASA TR R 6, 1959.

[6]Abel-Fattah, A. M., "Discrete Tone Emission from High Pressure Ratio Supersonic Jets from Convergent-Divergent Nozzles," *AIAA Journal*, Vol. 26, No. 3, 1988, pp. 283–291.

[7]Dash, S. M., and Wolf, D. F., "Fully Coupled Analysis of Jet Mixing Problem, Part 1, Shock Capturing Model, SCIPVIS," NASA CR 3761, Jan. 1984.

[8]Sinha, R., Zakky, V., and Erdos, J., "Flowfield Analysis of Plumes of Two Dimensional Underexpanded Jets by a Time Dependent Method," *AIAA Journal*, Vol. 9, No. 12, 1970, pp. 2363–2370.

[9]Dash, S. M., Pearce, B. E., and Pergament, H. S., "Prediction of Rocket Plume Flowfields for IR Signatures Studies," *Journal of Spacecraft and Rockets*, Vol. 17, No. 3, 1980, pp. 190–199.

[10]Lamont, P. J., and Hunt, B. L., "Impingement of Underexpanded Axisymmetric Jets on Perpendicular and Inclined Flat Plate," *Journal of Fluid Mechanics*, Vol. 100, Pt. 3, 1980, pp. 471–511.

[11]Jennions, I. K., and Hunt, B. L., "The Axisymmetric Impingement of Supersonic Air Jets on Cones," *Aeronautical Quarterly*, Vol. 31, Feb. 1980, pp. 26–41.

[12]Jameson, A., Schmidt, W., and Turkel, E., "Numerical Solution of Euler Equations by Finite Volume Method Using Runge-Kutta Time-Stepping Scheme," AIAA Paper 81-1259, June 1981.

Solution of Keller's Box Equations for Direct and Inverse Boundary-Layer Problems

Tarek M. A. El-Mistikawy*
Cairo University, Giza 12211, Egypt

Introduction

THE difference equations that result from applying Keller's box scheme to the direct boundary-layer problem have tradi-

Received May 17, 1993; revision Dec. 23, 1993; accepted for publication Dec. 30, 1993.

*Lecturer, Department of Engineering Mathematics and Physics, Faculty of Engineering.